

# Range Doppler and Image Autofocusing for FMCW Inverse Synthetic Aperture Radar

E. GIUSTI

M. MARTORELLA, Senior Member, IEEE  
University of Pisa

**Inverse synthetic aperture radar (ISAR) is a well-known technique for obtaining high-resolution radar images. ISAR techniques have been successfully applied in the recent past in combination with pulsed coherent radar. In order to be more appealing to both civilian and military fields, imaging sensors are required to be low cost, low powered, and compact. Coherent pulsed radars do not account for these requirements as much as frequency modulated continuous wave (FMCW) radars. However, FMCW radars transmit a linear frequency modulated (LFM) sweep in a relatively long time interval when compared with the pulse length of a coherent pulse radar. During such an interval the assumption of stop&go is no longer valid, that is the target cannot be considered stationary during the acquisition of the entire sweep echo. Therefore, the target motion within the sweep must be taken into account. Such a problem is formulated and solved for ISAR systems, where the target is noncooperative and additional unknowns are added to the signal model. In the present work, the authors define a complete FMCW-ISAR received signal model, propose an ISAR image formation technique suitable for FMCW radar and derive the point spread function (PSF) of the imaging system. Finally, the proposed FMCW ISAR autofocusing algorithm is tested on simulated and real data.**

Manuscript received September 24, 2009; revised August 6, 2010; released for publication October 11, 2010.

IEEE Log No. T-AES/47/4/942903.

Refereeing of this contribution was handled by P. Lombardo.

Authors' address: Dept. of Information Engineering,  
University of Pisa, via Caruso 16, Pisa, 56126, Italy, E-mail:  
(m.martorella@iet.unipi.it).

0018-9251/11/\$26.00 © 2011 IEEE

## I. INTRODUCTION

Interest in radar imaging is growing both in civilian and military fields. To make radar imagery applicable in vast scenarios, the radar sensor must be low cost, low weight, and low powered. Recent technology and signal processing developments have led to frequency modulated continuous wave (FMCW) sensors, which meet such requirements. As demonstrated in [1]–[5], FMCW waveforms can be used to form synthetic aperture radar (SAR) images. The image processing required for forming SAR images differs from the conventional SAR processing [3, 6]. Such a difference is dictated by the stop&go condition, which is no longer valid for FMCW radars. The usual SAR signal processing can be restored once the frequency offset introduced in the data is corrected for. In a SAR configuration, where the radar-target geometry is known a priori, such correction becomes reasonably straightforward.

In inverse SAR (ISAR) systems [7, 8], the radar-target geometry is not known a priori. Therefore, the required data correction cannot be performed in a simple manner. In this paper firstly, the received signal model for FMCW-ISAR systems is defined based on physical principles. Then the image formation problem is addressed and the imaging system point spread function (PSF) is analytically derived.

The ISAR autofocusing problem [9–13], which is part of the image formation, is also detailed in order to account for the continuous nature of the received signal. Moreover, the image distortions introduced by the use of FMCW radars are analysed when forming the ISAR image by means of a range-Doppler (RD) technique.

The problem of target radial motion compensation becomes more complex in FMCW ISAR since the number of phase terms to be estimated is considerably higher than in pulsed radar. This is because the phase is not stationary within one radar sweep. Therefore, each received signal sample phase must be estimated. The parametric algorithm proposed in this paper proposes a solution that allows estimating the phase history without increasing the computational complexity.

It must be mentioned that the problem of estimating the phase of all received signal samples also arises in pulsed stepped frequency ISAR systems, where the stop&go assumption is not valid [14, 15].

The effectiveness of the proposed autofocusing algorithm is tested both on simulated FMCW ISAR data and on real pulsed stepped frequency ISAR data.

The remainder of the paper is organised as follows. Section II details the FMCW-ISAR received signal modelling. The FMCW ISAR image formation processing is derived in Section III. Finally the results obtained by using both simulated and real data are shown in Sections IV and V.

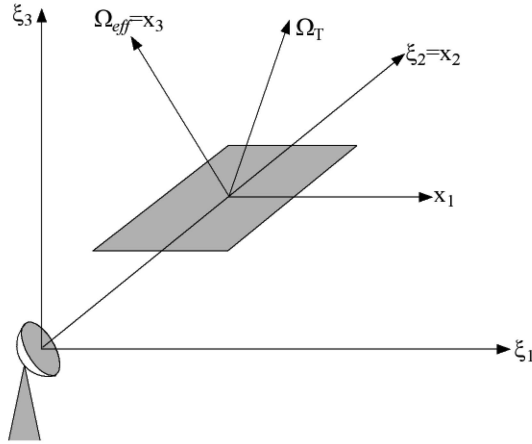


Fig. 1. Radar target geometry.

## II. FMCW-ISAR RECEIVED SIGNAL MODEL

The received signal model is defined by considering the radar-target geometry and the transmitted signal waveform, which in this case is assumed to be an FMCW signal. Let the geometry be represented by Fig. 1 and  $T_x(x_1, x_2, x_3)$  be a Cartesian reference system embedded on the target. By considering a Cartesian reference system embedded on the radar, namely  $T_\xi(\xi_1, \xi_2, \xi_3)$ , a rotation vector  $\Omega_T(t)$  can be defined as the total target angular rotation with respect to the radar. The effective rotation vector  $\Omega_{\text{eff}}(t)$  is the rotation vector component that contributes to the synthetic aperture formation. This latter can be obtained from the target rotation vector by applying a simple vector product, specifically  $\Omega_{\text{eff}}(t) = \mathbf{i}_{\text{LOS}}(t) \times [\Omega_T(t) \times \mathbf{i}_{\text{LOS}}(t)]$ , where  $\mathbf{i}_{\text{LOS}}(t)$  is the radar line of sight unit vector [16].

The transmitted waveform is assumed to be a sawtooth FM. Therefore, the instantaneous transmitted frequency can be expressed for each frequency sweep as follows

$$f(t_S) = f_c + \alpha t_S \quad (1)$$

where  $f_c$  is the carrier frequency,  $\alpha = \Delta f/T_S$  is the frequency sweep rate,  $\Delta f$  is the frequency sweep,  $T_S$  is the sweep repetition interval, and where  $t_S \in [-(T_S/2) \div (T_S/2)]$  is the time interval covered by a single frequency sweep.

Let  $S_T(t)$  be the analytical transmitted signal as defined in (2) [17]

$$S_T(t) = \sum_{n=-N}^N S_T(t_S, n) \quad (2)$$

where  $t \in [-(T_{\text{obs}}/2) \div (T_{\text{obs}}/2)]$ , the observation time is chosen to be a multiple of the FMCW period, specifically  $T_{\text{obs}} = (2N+1)T_S$ ,  $n \in [-N, \dots, N]$  represents the  $n$ th sweep,  $2N+1$  is the number of transmitted sweeps within  $T_{\text{obs}}$ , and

$$S_T(t_S, n) = A_T e^{j2\pi[f_c + (\alpha/2)t_S]t_S} \cdot \text{rect}\left(\frac{t_S - nT_S}{T_S}\right) \quad (3)$$

where  $A_T$  is a complex value that takes into account the signal energy and the initial phase and  $\text{rect}(t/T)$  is equal to 1 for  $|t| < T/2$ . It is worth pointing out that the FMCW transmitted signal is a periodic signal with period equal to  $T_S$ .

Therefore, the received signal in free space conditions, is given by

$$S_R(t) = \sum_{n=-N}^N S_R(t_S, n) \quad (4)$$

where

$$S_R(t_S, n) = K \int_V g(\xi) S_T(t_S - \tau(\xi, t_S, n), n) d\xi \quad (5)$$

where  $K$  is a complex amplitude depending on the radar equation,  $\tau(\xi, t_S, n) = 2R(\xi, t, n)/c$ ,  $c$  is the light speed in vacuum, and  $V$  is the spatial domain where the target's reflectivity function  $g(\xi)$  is defined.  $R(\xi, t, n)$  is the modulus of  $\mathbf{R}(\xi, t, n)$ , which is the vector that locates the position of an arbitrary point on the target. The time-varying coordinates of  $\mathbf{R}(\xi, t, n)$ , namely  $(\xi_1, \xi_2, \xi_3)$ , are defined with respect to the radar reference system. It is worth pointing out that the received signal is expressed as a function of the two variables  $t_S$  and  $n$  in order to be able to refer to the fast time  $t_S$  and the frequency sweep  $n$  separately.

In a typical ISAR scenario, we can assume that the target size is much smaller than the radar-target distance, therefore the straight iso-range approximation can be applied

$$R(\xi, t_S, n) \approx R_0(t_S, n) + \mathbf{x}^T \cdot \mathbf{i}_{\text{LOS}}(t_S, n) \quad (6)$$

where  $R_0(t_S, n)$  is the distance between an arbitrary point O on the target and the radar at the  $n$ th sweep and at time  $t_S$ ,  $\mathbf{i}_{\text{LOS}}(t_S, n)$  is the column unit vector of  $\mathbf{R}_0(t_S, n)$  and both  $\mathbf{x}$  and  $\xi$  represent the position of the same point on target in  $T_x$  and  $T_\xi$ , respectively.

By defining

$$\begin{aligned} \tau(t_S, n, \mathbf{x}) &= \frac{2}{c} (R_0(t_S, n) + \mathbf{x}^T \cdot \mathbf{i}_{\text{LOS}}(t_S, n)) \\ &= \tau_0(t_S, n) + \tau'(t_S, n, \mathbf{x}) \end{aligned} \quad (7)$$

where

$$\tau_0(t_S, n) = \frac{2}{c} R_0(t_S, n) \quad (8)$$

$$\tau'(t_S, n, \mathbf{x}) = \frac{2}{c} \mathbf{x}^T \cdot \mathbf{i}_{\text{LOS}}(t_S, n) \quad (9)$$

(5) can be rewritten as follows

$$S_R(t_S, n) = K \int_V g(\mathbf{x}) S_T(t_S - \tau_0(t_S, n) - \tau'(t_S, n, \mathbf{x}), n) d\mathbf{x} \quad (10)$$

where  $g(\mathbf{x})$  is the reflectivity function expressed with respect to the coordinate systems embedded on the target.

### III. FMCW-ISAR SIGNAL PROCESSING

Conventional ISAR systems make use of coherent pulsed radars [7, 8, 12, 18]. When a pulsed radar is used, the stop&go approximation can be made in order to simplify the image formation processing. In the case of FMCW-ISAR, the stop&go approximation is no longer valid because of the continuous nature of transmitted waveform. In this scenario, the target motions must be considered also with respect to the fast time  $t_s$ . It is worth pointing out that the effect of the stop&go approximation becomes more evident in the case of fast target motions.

Firstly, the radial motion compensation problem is discussed when using FMCW and then the system PSF is derived.

#### A. Radial Motion Compensation

For a relatively short observation time  $T_{\text{obs}}$  and relatively smooth target motions, the radar-target distance can be expressed by means of a quadratic form, as follows

$$R_0(t) = R_0 + v_R t + \frac{a_R}{2} t^2 \quad (11)$$

where  $v_R$  and  $a_R$  are, respectively, the radial velocity and acceleration of the target. The proposed autofocusing algorithm is going to estimate both the target motion parameters  $v_R$  and  $a_R$ . Because the last step of the classical RD image reconstruction technique is a two-dimensional Fourier transform,  $R_0$  only produces a shift along the range coordinate and does not affect the image focusing [12].

During the  $n$ th sweep interval, the radar-target distance is a function of time  $t_S$ , as defined by (12)

$$\begin{aligned} R_0(t_S, n) &= R_0 + v_R(t_S + nT_S) + \frac{a_R}{2}(t_S + nT_S)^2 \\ &\simeq R_0 + v_R n T_S + \frac{a_R}{2}(nT_S)^2 + (v_R + a_R n T_S)t_S. \end{aligned} \quad (12)$$

The approximation in (12) is effective when the following inequality applies

$$\frac{a_R}{2} T_S \ll v_R. \quad (13)$$

By defining the target's position and velocity at time instants  $nT_S$  as

$$R_0(n) = R_0 + v_R n T_S + \frac{a_R}{2}(nT_S)^2 \quad (14)$$

$$v_R(n) = v_R + a_R n T_S \quad (15)$$

(12) can be rewritten as follows

$$R_0(t_S, n) = R_0(n) + v_R(n)t_S. \quad (16)$$

After demodulation, the beat signal can be written as follows

$$S_b(t_S, n) = \beta S_T^*(t_S, n) S_R(t_S, n) \quad (17)$$

where  $\beta \in \mathbb{R}^+$  is a amplitude factor introduced by the demodulator and  $\beta \ll 1$ . By substituting (3) and (5) into (17) the beat signal can be expressed as follows [19]

$$\begin{aligned} S_b(t_S, n) &= K' \cdot \int_V g(\mathbf{x}) \exp [j2\pi(f_c + (\alpha/2)(t_S - \tau(t_S, n, \mathbf{x}))) \\ &\quad \cdot (t_S - \tau(t_S, n, \mathbf{x}))] \\ &\quad \cdot \exp [-j2\pi(f_c + (\alpha/2)t_S)t_S] \\ &\quad \cdot w(t_S, \tau(t_S, n, \mathbf{x}), n, T_S) d\mathbf{x} \end{aligned} \quad (18)$$

where  $K' = K \cdot \beta$  is a complex amplitude,  $|A_T|^2$  is included in  $K$  and

$$\begin{aligned} w(t_S, \tau(t_S, n, \mathbf{x}), n, T_S) &= w_T(t_S, n, T_S) \cdot w_R(t_S, \tau(t_S, n, \mathbf{x}), n, T_S) \\ &\equiv w_T(t_S, n, T_S) \end{aligned} \quad (19)$$

where the radar parameters are usually designed such that  $\tau(t_S, n, \mathbf{x}) \ll T_S$  and where  $w_T(t_S, n, T_S) = \text{rect}((t_S - nT_S)/T_S)$  and  $w_R(t_S, \tau(t_S, n, \mathbf{x}), n, T_S) = \text{rect}((t_S - nT_S - \tau(t_S, n, \mathbf{x}))/T_S)$ .

Therefore the beat signal can be rewritten as

$$\begin{aligned} S_b(t_S, n) &= K' w_T(t_S, n, T_S) \\ &\quad \cdot \int_V g(\mathbf{x}) \exp [j2\pi(f_c + (\alpha/2)(t_S - \tau(t_S, n, \mathbf{x}))) \\ &\quad \cdot (t_S - \tau(t_S, n, \mathbf{x}))] \\ &\quad \cdot \exp [-i2\pi(f_c + (\alpha/2)t_S)t_S] d\mathbf{x} \end{aligned} \quad (20)$$

By substituting (7) into (20) the beat signal can be rewritten as follows

$$\begin{aligned} S_b(t_S, n) &= K' w_T(t_S, n, T_S) \cdot e^{j(\phi_0(t_S, n))} \\ &\quad \cdot \int_V g(\mathbf{x}) \exp [j(\phi_1(t_S, n, \mathbf{x}) + \phi_2(t_S, n, \mathbf{x}))] d\mathbf{x} \end{aligned} \quad (21)$$

where

$$\phi_0(t_S, n) = -2\pi(f_c + \alpha t_S)\tau_0(t_S, n) + \pi\alpha\tau_0^2(t_S, n) \quad (22)$$

$$\phi_1(t_S, n, \mathbf{x}) = -2\pi(f_c + \alpha t_S) \cdot \tau'(t_S, n, \mathbf{x}) \quad (23)$$

$$\begin{aligned} \phi_2(t_S, n, \mathbf{x}) &= \pi\alpha(\tau'(t_S, n, \mathbf{x}))^2 \\ &\quad + 2\pi\alpha\tau_0(t_S, n)\tau'(t_S, n, \mathbf{x}). \end{aligned} \quad (24)$$

It is worth pointing out that the demodulated signal up-conversion component has been omitted from (20) since it falls outside the receiver's bandwidth and therefore it is filtered out.

Since in practice  $f_D \ll f_c$  [5], where  $f_D$  is the target Doppler frequency and it depends on the target radial velocity, as defined in (27), the major effect of the target motion is a Doppler frequency shift. With these

assumptions and using (16)

$$\begin{aligned}\phi_0(t_S, n) \approx & -2\pi f_c \tau_0(n) - 2\pi f_D(n)t_S - 2\pi f_b(n)t_S \\ & - 2\pi\alpha \frac{f_D(n)}{f_c} t_s^2 + \pi\alpha\tau_0^2(n)\end{aligned}\quad (25)$$

where

$$\tau_0(n) = \frac{2}{c} R_0(n) \quad (26)$$

$$f_D(n) = \frac{2f_c v_R(n)}{c} \quad (27)$$

$$f_b(n) = \alpha\tau_0(n). \quad (28)$$

Equation (25) is derived in the Appendix. The term  $\pi\alpha\tau_0^2(n)$  is known as the Residual Video Phase (RVP). The compensation of the RVP is possible although in most cases the effect of this term is negligible [20, 5].

Since the target's radial speed can be assumed constant during the sweep time, also the frequency Doppler shift can be assumed constant in the same interval. Therefore, the frequency response is only shifted in range without being affected by significant distortions. However, the variations of the Doppler frequency shift and that of the phase term  $\phi_0(t_S, n)$  cause a range migration that must be accounted for.

In order to compensate the target radial motion, the phase term outside the integral in (21), namely  $\phi_0(t_S, n)$ , must be estimated and removed. In ISAR scenarios, where the target is usually noncooperative, this operation is done by means of autofocusing algorithms. This aspect is detailed in the next section.

## B. Autofocusing Algorithm

The estimation of  $\phi_0(t_S, n)$  resorts to the estimation of the target radial motion parameters, namely  $v_R$  and  $a_R$ . As demonstrated in [12] the parameter  $R_0$  does not affect the image focus.

After a perfect radial motion compensation, the beat signal can be expressed in (29), where  $w_T(t_S, n, T_S)$  has been omitted for notation simplicity

$$S_{bc}(t_S, n) = K' \int_V g(\mathbf{x}) e^{j(\phi_1(t_S, n, \mathbf{x}) + \phi_2(t_S, n, \mathbf{x}))} d\mathbf{x}. \quad (29)$$

Let  $\Theta = [v_R, a_R]$  be the vector containing the unknowns and  $\phi_0(t_S, n; \Theta)$  be the relative phase term obtained by substituting the unknowns with those in  $\Theta$ . The radial motion compensation problem can be recast as an optimisation problem where the image contrast (IC) is maximised with respect to the unknown vector  $\Theta$ , as defined in (30).

$$\hat{\Theta} = \arg \max_{\Theta} \{ \text{IC}[\Theta] \} \quad (30)$$

where

$$\text{IC}[\Theta] = \frac{\sqrt{E\{[I(\Theta) - E[I(\Theta)]]^2\}}}{E[I(\Theta)]}$$

and where  $I(\Theta)$  is the ISAR image formed after compensating the beat signal with the phase term  $\phi_0(t_S, n; \Theta)$ , as formalised in (31).

$$I(\Theta) = |\text{RD}\{S_b(t_S, n) \cdot e^{-j\phi_0(t_S, n; \Theta)}\}| \quad (31)$$

where  $\text{RD}\{\cdot\}$  indicates the operation of image formation by means of an RD approach, as clarified in Section IIIC. In the remainder of this paper, such a radial motion compensation will be addressed as FMCW ISAR autofocusing algorithm and will be distinguished from the conventional ISAR autofocusing algorithm [12].

As stated in Section IIIA, conventional ISAR systems make use of coherent pulsed radars. For such systems the stop&go approximation can be made in order to simplify the image formation process. Therefore by exploiting such assumption and by using the straight iso-range approximation, the radar-target distance in (6) can be approximated as follows:

$$R^{(P)}(\xi, n) \approx R_0(n) + \mathbf{x}^T \cdot \mathbf{i}_{\text{LOS}}(n) \quad (32)$$

where  $R_0(n)$  is defined in (14). Therefore the phase term that must be estimated and removed in order to focus the ISAR image, can be derived following the procedure described in Section IIIA and can be expressed as follows

$$\phi_0^{(P)}(n) = -2\pi f_c \tau_0(n) - 2\pi f_b(n)t_S + \alpha\pi\tau_0^2(n). \quad (33)$$

By comparing (25) and (33), it can be noted that the problem of radial motion compensation becomes more complex in FMCW radar since the number of phase terms to be estimated becomes equal to the product  $N'M'$ , where  $N' = 2N + 1$  is the number of slow-time samples and  $M' = T_S F_{\text{samp}}$  is the number of fast-time samples. It must be specified that  $F_{\text{samp}}$  is the sampling frequency used to digitise the received signal. It is worth pointing out that the sampling frequency  $F_{\text{samp}}$  is defined according to the desired range ambiguity  $\Delta R$ , where the latter depends on the sampling frequency by means of  $\Delta R = c/2F_{\text{samp}}$ .

## C. Point Spread Function

The RD technique is the conventional method used for reconstructing ISAR images. Such a technique is based on the assumption that the Doppler frequency of each scatterer, relative to a reference point taken on the target, is constant within the observation time. The assumption of stationary Doppler components is usually satisfied when the effective rotation vector  $\Omega_{\text{eff}}(t)$  is constant within the observation time and the coherent processing interval (CPI) is kept short. This assumption is considered satisfied in the remainder of this paper.

The expression of the received signal model given in (10) is considered in order to derive the imaging system PSF.

By considering the separability of translational and rotational motions for a rigid body, the target rotation can be referred to an axis passing through point O.

Let  $\theta(t_s, n)$  be the target aspect angle at any given time  $t_s$  and radar sweep  $n$  and let  $T_x$  be defined such that the  $x_3$  axis is aligned with  $\Omega_{\text{eff}}$ . The latter is not constraining the problem since the choice of the orientation of the reference system embedded on the target is fully arbitrary.

With these assumptions, the scalar product between the vector defining the position of a point scatterer and the unit vector of the LOS at the  $n$ th sweep and at a generic instant time  $t_s$ , can be written as follows:

$$\mathbf{x}^T \cdot \mathbf{i}_{\text{LOS}}(t_s, n) = x_1 \cos(\theta(t_s, n)) + x_2 \sin(\theta(t_s, n)). \quad (34)$$

By substituting (23), (24), and (7) into (29) and by assuming that  $f_D \ll f_c$ , the beat signal after motion compensation can be approximated as follows, where  $w_T(t_s, n, T_S)$  has been omitted for notation simplicity:

$$\begin{aligned} S_{bc}(t_s, n) \\ = K' \int g'(\mathbf{x}') \cdot \exp[-j2\pi[x_1 X_1(t_s, n) + x_2 X_2(t_s, n)]] d\mathbf{x}' \end{aligned} \quad (35)$$

where  $X_1(t_s, n)$  and  $X_2(t_s, n)$  are defined as follows and are derived in the Appendix

$$\begin{aligned} X_1(t_s, n) &= \left\{ f_c + \alpha \left[ t_s - \tau_0(n) - \frac{\tau'(t_s, n, \mathbf{x}')}{2} \right] \right\} \\ &\cdot \frac{2}{c} \cos(\theta(t_s, n)) \end{aligned} \quad (36)$$

$$\begin{aligned} X_2(t_s, n) &= \left\{ f_c + \alpha \left[ t_s - \tau_0(n) - \frac{\tau'(t_s, n, \mathbf{x}')}{2} \right] \right\} \\ &\cdot \frac{2}{c} \sin(\theta(t_s, n)) \end{aligned} \quad (37)$$

and where  $g'(x_1, x_2) = \int g(\mathbf{x}) dx_3$  and  $\mathbf{x}' = (x_1, x_2)$ . It must be clarified that the integral in (35) is a two-dimensional integral and  $\tau'(t_s, n, \mathbf{x}') = \tau'(t_s, n, \mathbf{x})$  since the LOS is always orthogonal to the  $x_3$  axis (as a result of the choice of an arbitrary reference system embedded on the target).

When the effective rotation vector  $\Omega_{\text{eff}}$  can be considered constant, the analytical expression of the aspect angle  $\theta(t_s, n)$  is linear with respect to time.

$$\theta(t_s, n) \simeq \Omega_{\text{eff}}(t_s + nT_s). \quad (38)$$

The RD technique can be successfully be implemented by means of a Fourier transform (FT) when the polar grid in the Fourier domain can be approximated by a rectangular grid. Such an approximation can be assumed valid when [8, 7, 21]:

$$\left| \theta(t_s, n) - \frac{\pi}{2} \right| \ll 1. \quad (39)$$

Under the assumption expressed in (38), (36)–(37) can be rewritten as follows

$$\begin{aligned} X_1(t_s, n) &= \frac{2}{c} (\Omega_{\text{eff}}(t_s + nT_S)) \\ &\cdot \left\{ f_c + \alpha \left[ t_s - \tau_0(n) - \frac{\tau'(t_s, n, \mathbf{x})}{2} \right] \right\} \end{aligned} \quad (40)$$

$$X_2(t_s, n) = \frac{2}{c} \left\{ f_c + \alpha \left[ t_s - \tau_0(n) - \frac{\tau'(t_s, n, \mathbf{x})}{2} \right] \right\}. \quad (41)$$

A closed-form derivation of the system PSF can be obtained in the case of narrowband FMCW ISAR systems, where the following assumption can be made

$$\alpha \left[ t_s - \tau_0(n) - \frac{\tau'(t_s, n, \mathbf{x})}{2} \right] \ll f_c. \quad (42)$$

After applying (42), (40), and (41) can be rewritten as follows

$$X_1(t_s, n) \cong \frac{2f_c}{c} (\Omega_{\text{eff}}(t_s + nT_S)) \quad (43)$$

$$X_2(t_s, n) \cong \frac{2}{c} (f_c + \alpha t_s). \quad (44)$$

By using (1),  $X_1(f, n)$  and  $X_2(f, n)$  can be expressed as follows

$$X_1(f, n) = \frac{2}{c} f_c \frac{\Omega_{\text{eff}}}{\alpha} (f - f_c) + \frac{2}{c} f_c \Omega_{\text{eff}} n T_S \quad (45)$$

$$X_2(f) = \frac{2}{c} f. \quad (46)$$

A relationship between  $X_1$  and  $X_2$  is obtained by substituting (46) into (45). The result is shown in (47):

$$X_1(X_2, n) = \frac{f_c \Omega_{\text{eff}}}{\alpha} X_2 - \frac{2f_c^2 \Omega_{\text{eff}}}{c\alpha} + \frac{2f_c \Omega_{\text{eff}} n T_S}{c}. \quad (47)$$

The window  $W(X_1, X_2)$  defines the domain where the reflectivity function FT exists. The analytical expression of  $W(X_1, X_2)$  is as follows:

$$W(X_1, X_2) = \begin{cases} 1 & \text{when } \begin{cases} -\frac{B}{2} + C \leq X_2 \leq +\frac{B}{2} + C \\ AX_2 + D - E \leq X_1 \leq AX_2 + D + E \end{cases} \\ 0 & \text{otherwise} \end{cases} \quad (48)$$

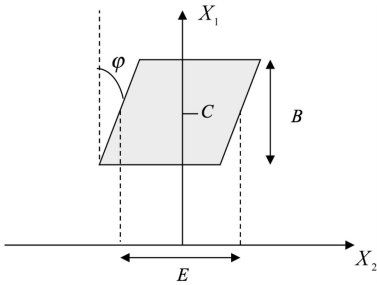


Fig. 2. FMCW-ISAR support band.

where

$$A = \tan(\varphi) = \frac{f_c \Omega_{\text{eff}}}{\alpha} \quad (49)$$

$$B = \frac{2\Delta f}{c}, \quad C = \frac{2f_c}{c} \quad (50)$$

$$D = -\frac{2f_c^2 \Omega_{\text{eff}}}{c\alpha}, \quad E = \frac{2f_c \Omega_{\text{eff}} N T_S}{c}. \quad (51)$$

Fig. 2 shows a qualitative example of  $W(X_1, X_2)$  in the 2-D Fourier domain.

In order to apply the RD operator and calculate the PSF, the motion compensated beat signal in (29) is rewritten as a function of the spatial frequency coordinates

$$\begin{aligned} S_{bc}(X_1, X_2) &= W(X_1, X_2) \int g'(x_1, x_2) e^{-j2\pi[x_1 X_1 + x_2 X_2]} dx_1 dx_2 \\ &= W(X_1, X_2) G'(X_1, X_2) \end{aligned} \quad (52)$$

where  $G'(X_1, X_2)$  is the 2D-FT of  $g'(x_1, x_2)$ .

The ISAR image can be obtained by applying the RD operator, which consists of a 2D-IFT (inverse FT):

$$S_{bc}(x_1, x_2) = w(x_1, x_2) \otimes \otimes g'(x_1, x_2) \quad (53)$$

where  $\otimes \otimes$  means the two-dimensional convolution. It is worth noting that also in the case of FMCW ISAR, the ISAR image can be interpreted as the linear convolution of the projection of the reflectivity function onto the image plane and the system PSF  $w(x_1, x_2)$ .

The window  $W(X_1, X_2)$  defines a parallelepiped on the spatial frequency plane. The characteristic angle  $\varphi$  depends on the modulus of the effective rotation vector, as shown in (49). The window  $W(X_1, X_2)$  approximates a rectangle when the effective rotation vector modulus is small.

The narrowband FMCW-ISAR system PSF is the 2D-FT of (48)

$$\begin{aligned} w(x_1, x_2) &= EB \operatorname{sinc}(x_1 E) \operatorname{sinc}((x_2 + Ax_1) B) \\ &\cdot e^{-j2\pi x_1 D} e^{-j2\pi(x_2 + Ax_1) D}. \end{aligned} \quad (54)$$

It must be pointed out that the distortion caused by the nonrectangular Fourier domain is not strong enough to seriously alter the sinc-like shape of an ideal ISAR PSF.

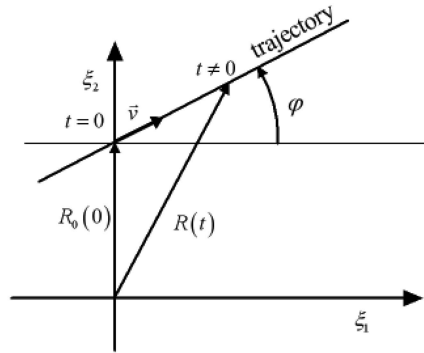


Fig. 3. Radar target geometry.

TABLE I  
Radar Parameters

$f_c$	$\Delta f$	$T_S$	$\delta_r$
10 GHz	500 MHz	5 ms	0.3 m

Simulated and real data results prove that well-focussed and nondistorted ISAR images can be produced when using suitable autofocusing techniques also in the case of invalidity of the stop&go assumption.

#### IV. SIMULATION RESULTS

It is demonstrated in this section that when the stop&go condition is not satisfied, such as in the case of FMCW radars, conventional ISAR image formation must be replaced by an FMCW ISAR image processing in order to obtain well-focused images.

##### A. Simulation Description

A target is supposed to be moving with velocity  $v$  along a rectilinear trajectory forming an angle  $\phi$  with the radar LOS as depicted in Fig. 3. The target, shown in Fig. 4, is composed of 35 ideal scatterers with identical reflectivity.

The radar parameters are shown in Table I.

##### B. Results

The received signal has been simulated for several values of the velocity  $v$ . The correspondent ISAR images have been focussed by using both the FMCW ISAR autofocusing algorithm, which takes into account the target motion within a sweep, and the conventional (pulsed) ISAR autofocusing algorithm. Fig. 5 shows the ISAR images of the target in the case of  $v = [50, 100, 150, 200, 250]$  m/s and  $\phi = 50^\circ$  obtained by using the FMCW ISAR autofocusing algorithm (left-hand column) and the conventional autofocusing algorithm (right-hand column). The number of transmitted sweeps depends on the target velocity  $v$  and it is set in order to have a cross-range resolution equal to  $\delta_{cr} = 1.45$  m [16]. It must be pointed out that the stop&go approximation is no

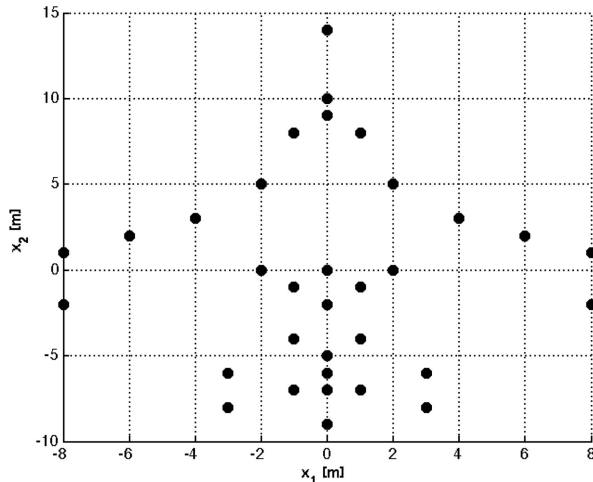


Fig. 4. Top view of target (left) and in the 3D space (right).

longer valid when FMCW radars are used, especially in the case of high target radial velocity. In particular, it can be noted that the radial target motion within each sweep causes a spreading of the PSF mainly along the range direction. In Fig. 6 where the range section of ISAR images (c) and (h) in Fig. 5 are shown, the spreading of the PSF along the range direction is more evident.

The image entropy (IE) value has also been used to assess the quality of the image. Therefore in Table II are reported the IE values of the ISAR images obtained by using both the FMCW ISAR autofocusing algorithm,  $IE^{(FM)}$ , and the conventional autofocusing algorithm,  $IE^{(C)}$  and shown in Fig. 5. Moreover the differences between the estimated and the actual values of target radial motion parameters are also shown in Table II. Specifically,  $(|\delta_{v_R}^{(FM)}|, |\delta_{a_R}^{(FM)}|)$  are, respectively, the difference between the actual radial velocity and acceleration and the estimated ones by using the FMCW ISAR autofocusing algorithm.  $(|\delta_{v_R}^{(C)}|, |\delta_{a_R}^{(C)}|)$  are, instead, the difference between the actual radial velocity and acceleration and the estimated ones by using the conventional autofocusing algorithm. As can be noted, the FMCW ISAR autofocusing algorithm estimates both  $v_R$  and  $a_R$  with more accuracy. The corresponding ISAR images have, therefore, higher contrast values and lower entropy values.

Fig. 7 shows the contrast values corresponding to the ISAR images shown in Fig. 5. It is worth highlighting that contrast values corresponding to the ISAR images obtained by using the FMCW ISAR autofocusing algorithm (solid black line) are always higher than those obtained by using the conventional autofocusing algorithm (dashed grey line), which confirms the visual analysis of Fig. 5. It is also important to note that even in a simple case of a target moving along a rectilinear trajectory, the ISAR image focus can be significantly decreased if conventional ISAR autofocusing algorithms are used.

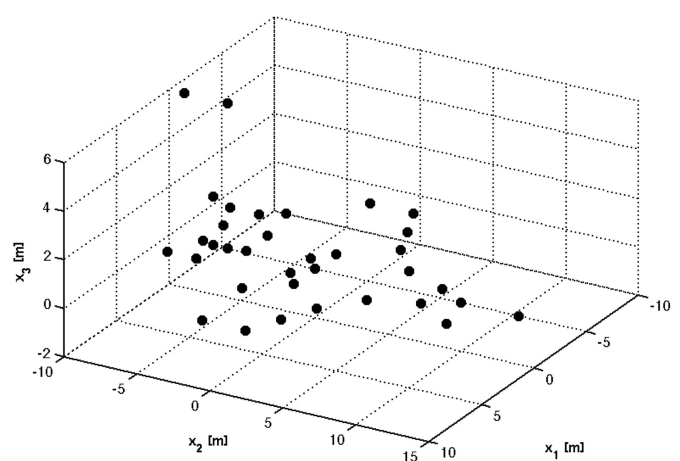


TABLE II

Estimated Target Radial Motion Parameters Accuracy and Image Entropy

$v$ [m/s]	$( \delta_{v_R}^{(FM)} ,  \delta_{a_R}^{(FM)} )$	$( \delta_{v_R}^{(C)} ,  \delta_{a_R}^{(C)} )$	$(IE^{(FM)}, IE^{(C)})$
50	(0.005, 0.021)	(0.179, 0.019)	(4.948, 7.465)
100	(0.073, 0.02)	(0.745, 0.04)	(4.638, 8.283)
150	(0.065, 0.043)	(0.169, 0.057)	(4.626, 8.833)
200	(0.027, 0.083)	(0.106, 0.095)	(4.614, 9.217)
250	(0.11, 0.116)	(1.118, 0.0151)	(4.592, 9.497)

TABLE III

Radar Parameters (Aircrafts)

M (No. of transmitted frequencies)	128
Lowest frequency	9.26 GHz
Frequency step	1.5–2 MHz
Range resolution	0.78-m
Radar height	ground level
targets type	Boeing 737-727
PRF	20 KHz

TABLE IV

Radar Parameters (Ships)

M (No. of transmitted frequencies)	256
Lowest frequency	9.16 GHz
Frequency step	0.6 MHz
Range resolution	0.97 m
Radar height	305 m
targets type	bulk loader–bulk carrier
PRF	20 KHz

## V. REAL DATA RESULTS

### A. Data Set

The data set used to test the algorithm performance were collected by using a low-power instrumented radar system developed by the Australian Defence Science & Technology Organisation (DSTO). Tables III and IV show the radar parameters used to collect the aircraft and the ship dataset, respectively

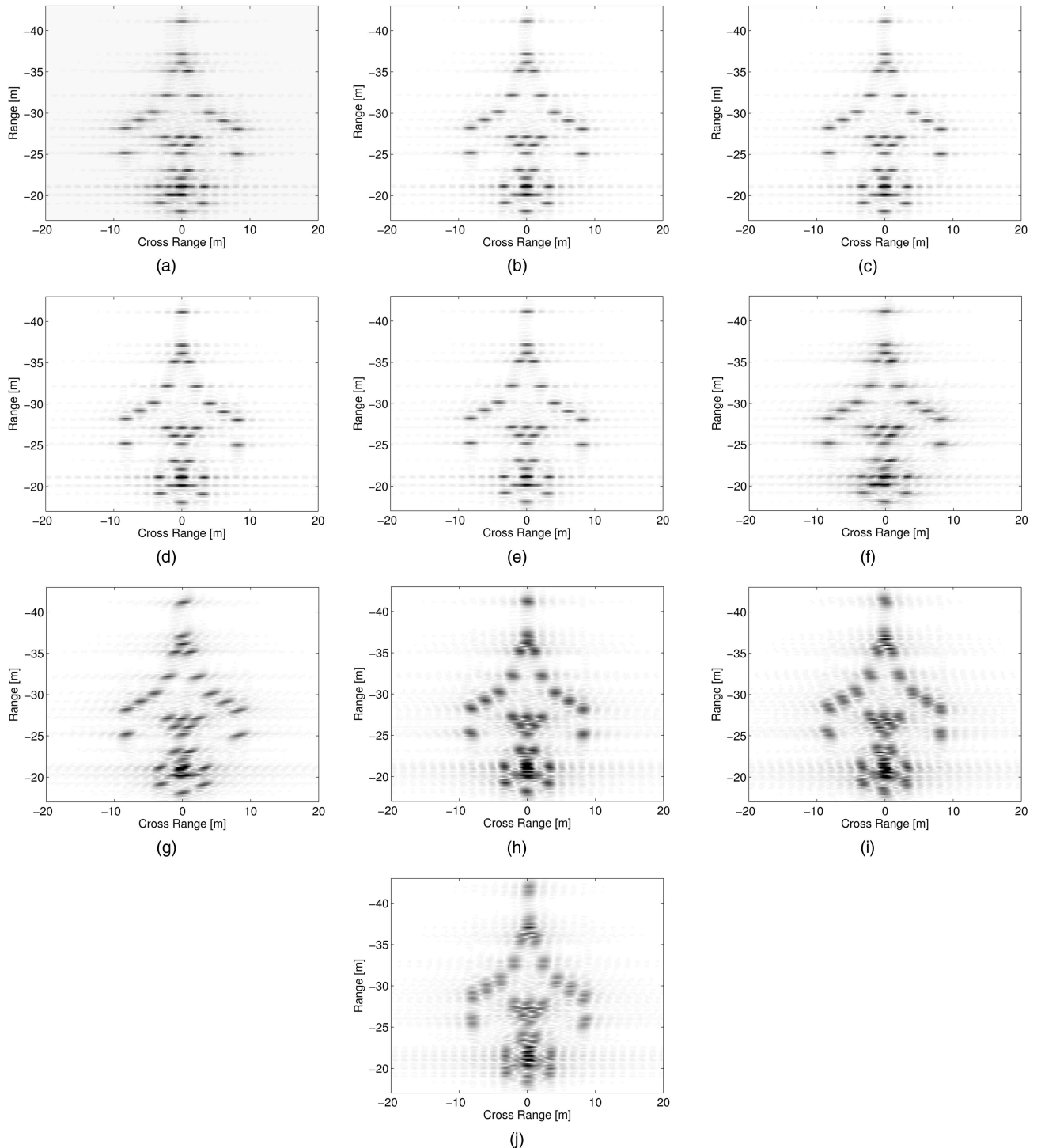


Fig. 5. ISAR images: (a)–(e) obtained by using FMCW ISAR autofocusing algorithm; (f)–(j) obtained by using the conventional autofocusing algorithm. (a)  $-v = 50$  m/s. (b)  $-v = 100$  m/s. (c)  $-v = 150$  m/s. (d)  $-v = 200$  m/s. (e)  $-v = 250$  m/s. (f)  $-v = 50$  m/s. (g)  $-v = 100$  m/s. (h)  $-v = 150$  m/s. (i)  $-v = 200$  m/s. (j)  $-v = 250$  m/s.

[17]. The first dataset was gathered by using a ground based radar, located near the Adelaide civilian airport. The illuminated targets are a Boeing 737 and a Boeing 727. The second data set has been acquired by an airborne radar illuminating a bulk carrier and a bulk loader (Fig. 8). In this case both the ship and the airplane motion contribute to the total aspect angle variation. Both data sets were acquired by using a

horizontally polarised transmit and receive antenna mounted on a pedestal that was pointed manually to track the targets. The aircraft dataset was gathered soon after take-off from Adelaide airport at ranges between 1.5 and 3 Km. The second data set was gathered as the C-130 aircraft carrying the radar flew away from the vessels at ranges between 1 and 6 Km. All the targets were illuminated for a long observation

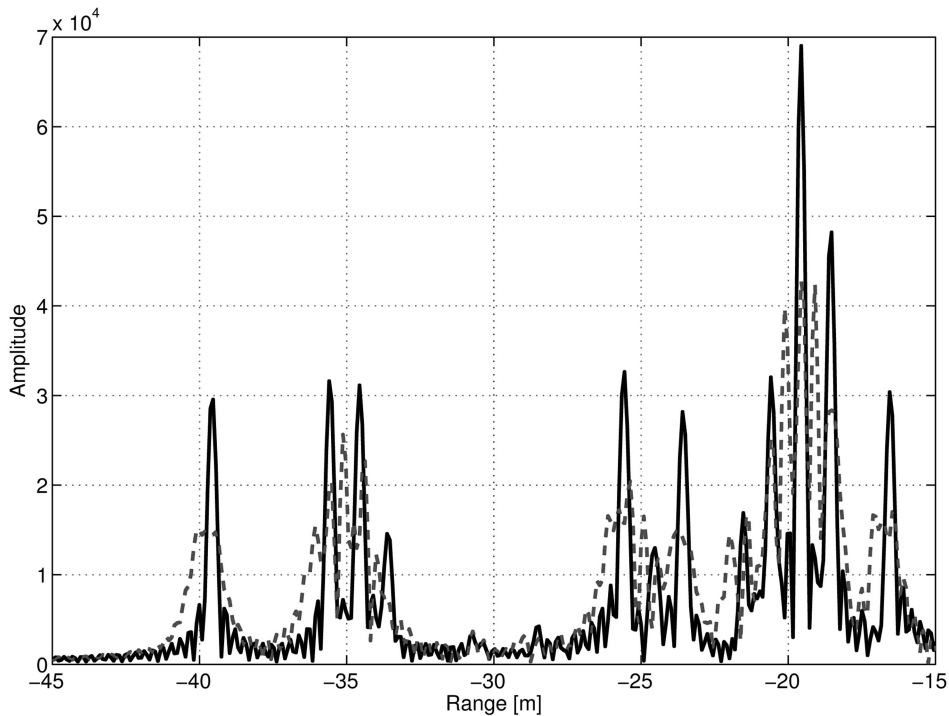


Fig. 6. Range sections at cross range = 0 m of ISAR iamges (c) and (h)—solid dark and grey line respectively.

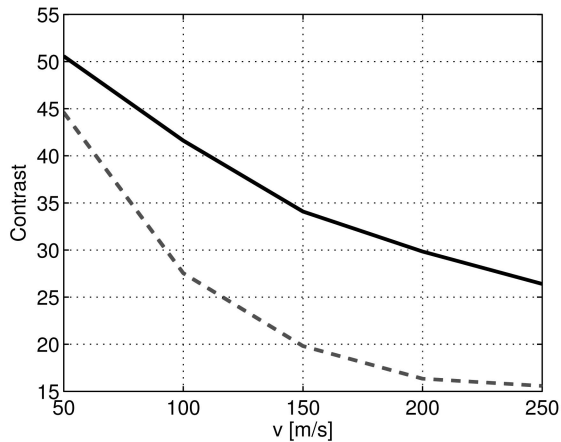


Fig. 7. Contrast values— $\phi = 50^\circ$ . Solid dark line represents IC values of images (a)–(e) in Fig. 5 and therefore is obtained by using the FMCW ISAR autofocus algorithm, whereas dashed grey line represents IC values of images (f)–(j) in Fig. 5 and therefore is obtained by using conventional autofocus algorithm.

time (about 1 min), therefore a shorter integration time has been chosen so that the assumption in (12) can be considered valid [22].

As already stated in Section I, the real data used to test the algorithm performance consists of stepped frequency waveforms. The equations of the LFMCW radar can be used in stepped frequency radar because the stepped frequency radar is a piecewise approximation of the LFMCW radar. Therefore, the assumption of stop&go is no longer valid and the target radial motion within the sweep must be taken into account.

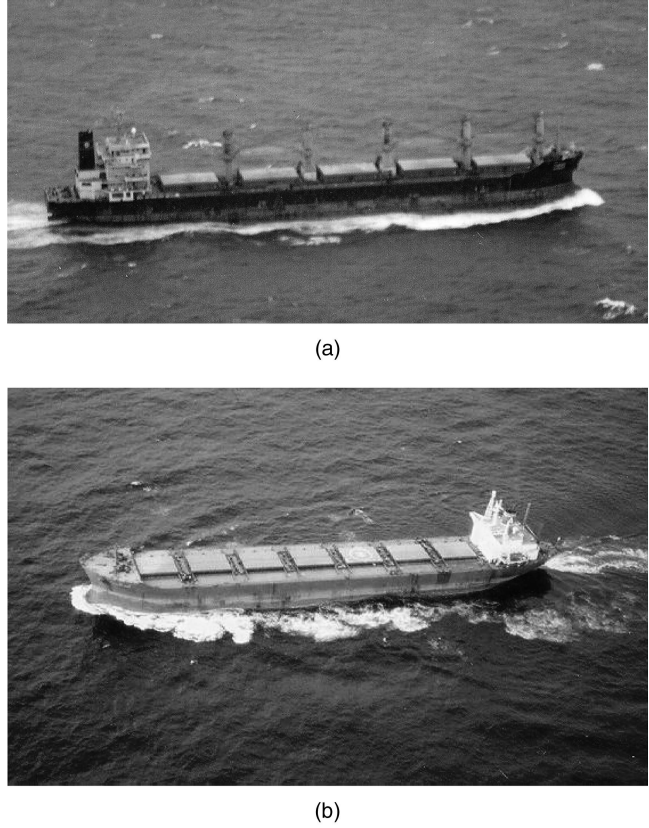


Fig. 8. (a) Bulk loader. (b) Bulk carrier.

## B. Results

The real data analysis has been performed by using both the FMCW ISAR autofocus algorithm and the conventional (pulsed) ISAR autofocus

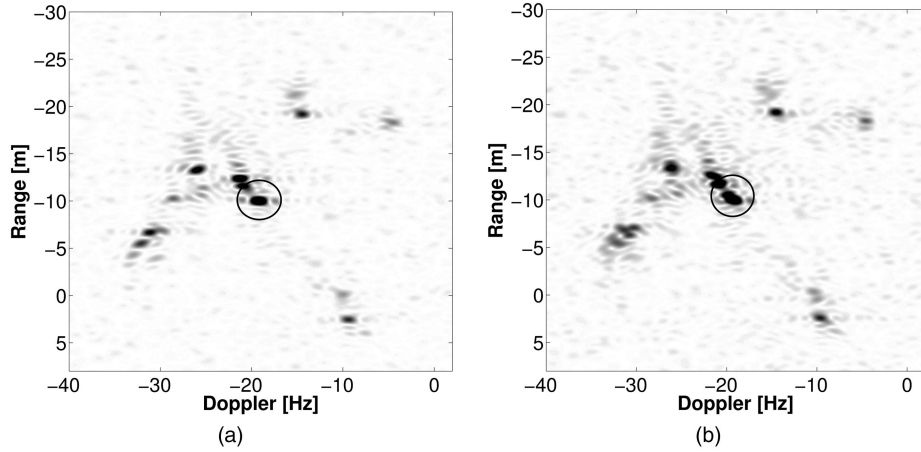


Fig. 9. Boeing 737 ISAR images obtained by using FMCW ISAR autofocusing algorithm (a) and conventional autofocusing algorithm (b).

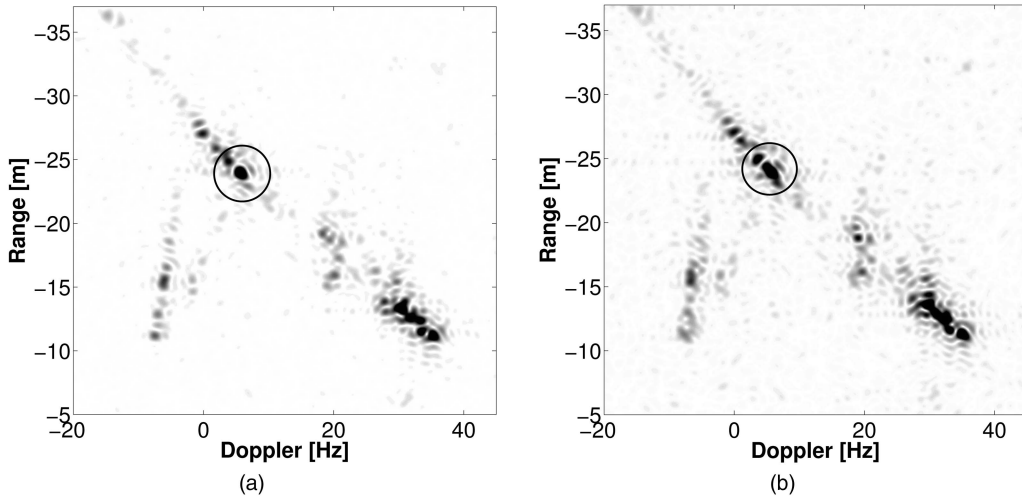


Fig. 10. Boeing 727 ISAR images obtained by using FMCW ISAR autofocusing algorithm (a) and conventional autofocusing algorithm (b).

algorithm. The comparison analysis between the two algorithms has been carried out by considering the image visual quality and the IC value. The function IC represents the normalised variance of the image intensity and provides a measure of the image focus [12].

1) *Aircraft*: The ISAR images of the Boeing 737 and the Boeing 727 are shown in Fig. 9 and Fig. 10, respectively, obtained by using both the FMCW ISAR autofocus algorithm (on the left) and the conventional ISAR autofocus algorithm (on the right).

It is possible to note by observing Fig. 9 and Fig. 10, that although both the autofocus algorithms are able to focus the ISAR images, the target radial motion within the sweep not compensated by using the conventional ISAR autofocus algorithm, produces a PSF spreading mostly along the range direction.

Such an effect is more evident when observing both the range and Doppler sections of the previous ISAR images for the highlighted scattering centre

TABLE V  
Peak and Contrast Values of the ISAR Images in Fig. 9 and Fig. 10

		FMCW ISAR	Pulsed ISAR
Boeing 737	Peak	62.18 dB	61.28 dB
	IC	0.8073	0.7977
	E	13.8203	13.8999
Boeing 727	Peak	61.44 dB	60.68 dB
	IC	1.0317	1.0278
	E	13.1168	13.1555

in Fig. 9 and Fig. 10, as shown in Fig. 11 and Fig. 12.

The black line and the grey line represent the range and Doppler sections of the ISAR images obtained by using the proposed and the conventional autofocus algorithm, respectively. The proposed autofocus algorithm shows a larger peak value. The peak value, the IC values and the entropy (E) values relative to the ISAR images in Fig. 9 and Fig. 10 are shown in Table V. It should be noted

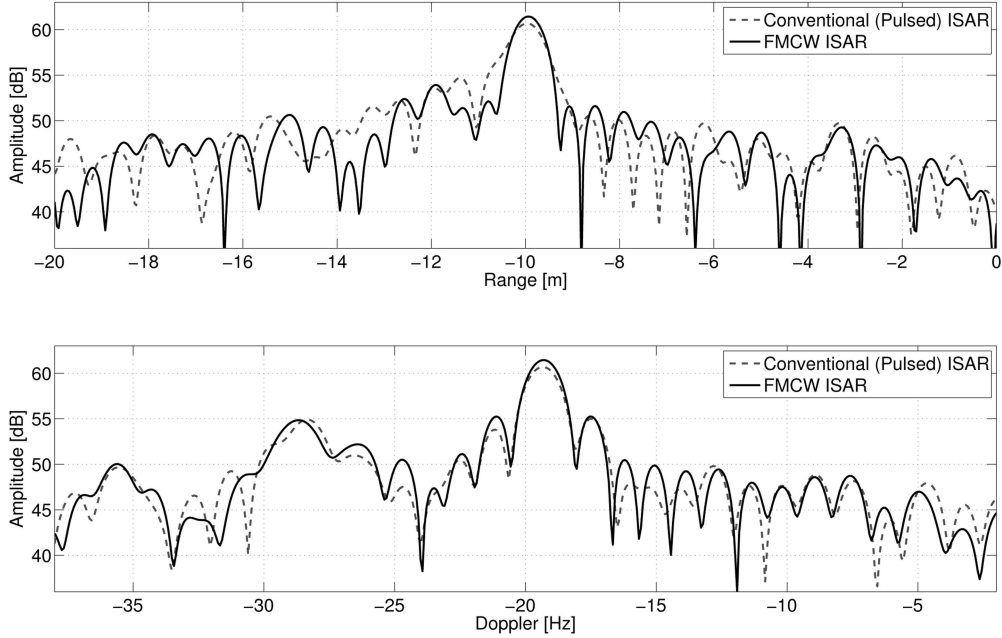


Fig. 11. Range and Doppler sections of Fig. 9 (a)–(b).

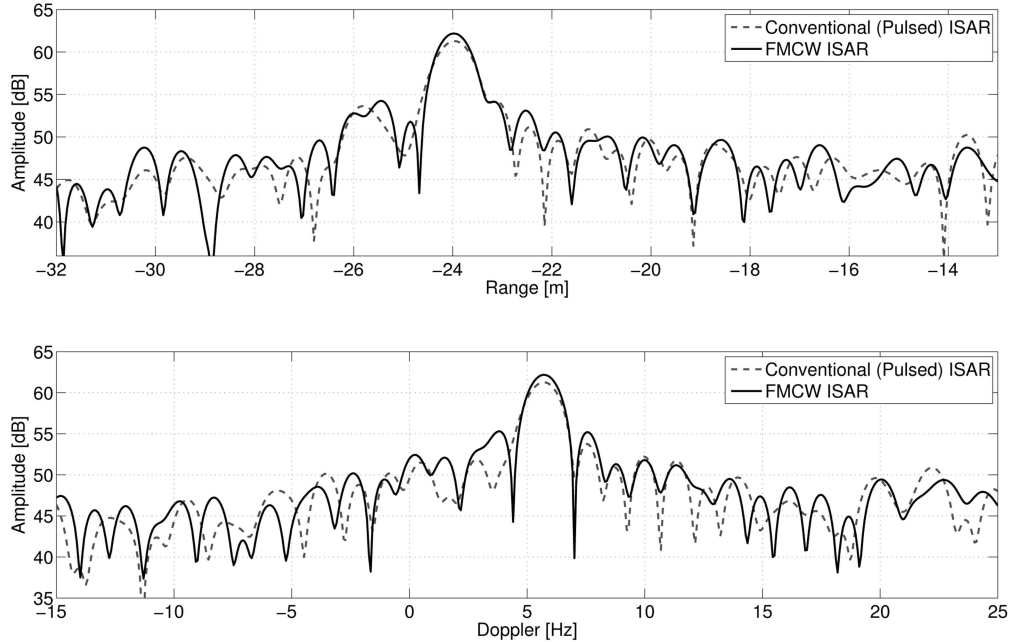


Fig. 12. Range and Doppler sections of Fig. 10 (a)–(b).

that the image peak (IP) value is an indicator of the image focus degree of only a local area in the image. Usually, a high value of the peak does not guarantee a good focus of the whole image. Nevertheless, when associated with a high IC, it can represent a good indicator of the image focus. In fact, an image defocusing provokes a scatterer energy spread, and hence it provokes a peak value decrease. It is worth pointing out that images with a higher IC value also have a lower value of E.

As previously stated, for long recorded data, the target rotation vector is far from being constant during the observation time. It is therefore necessary

to select one or more shorter integration time intervals to obtain one or more focused ISAR images of the target. Specifically the ISAR images shown previously have been obtained by selecting  $N = 128$  stepped frequency bursts from the dataset [22].

In order to compare the two autofocusing algorithms, it is necessary to compare the IC values of a large set of ISAR images. Therefore, a time moving window of 128 sweeps has been shifted along the data by 64 sweeps at each step. In Fig. 13 the black line represents the difference between  $IC_{FMCW}$ , which is the contrast value obtained by using the

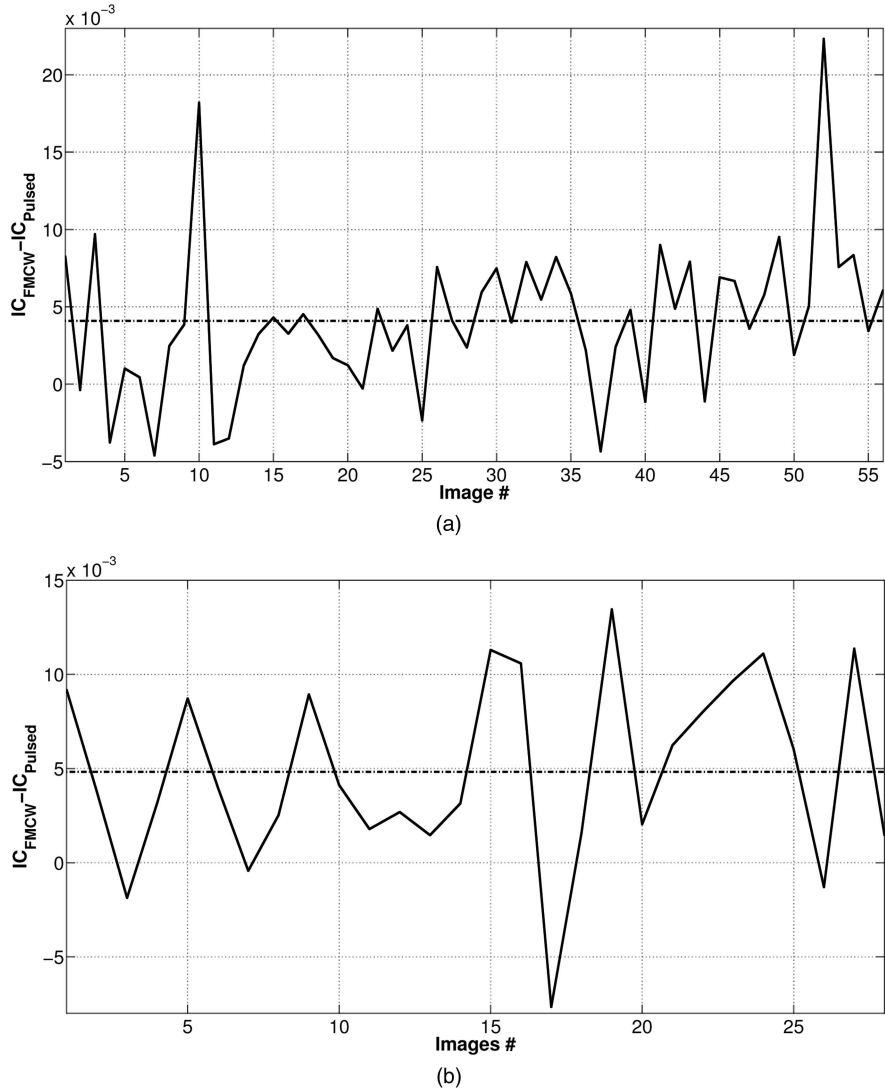


Fig. 13. Difference between  $IC_{FMCW}$  and  $IC_{Pulsed}$  for Boeing 737 (on top) and for Boeing 727 (on bottom).

TABLE VI  
Peak and Contrast Values of ISAR Images in Fig. 14 and Fig. 15

		FMCW ISAR	Pulsed ISAR
Bulk carrier	Peak	72.85 dB	71.91 dB
	IC	2.8023	2.5178
	E	9.7751	10.2512
Bulk loader	Peak	71.94 dB	71.3 dB
	IC	2.7124	2.6637
	E	10.2512	10.3854

FMCW ISAR autofocusing algorithm, and  $IC_{Pulsed}$ , which is the contrast value obtained by using the conventional ISAR autofocusing algorithm. The dashed line represents the mean value of such difference.

The results in Fig. 13 show that for almost all the inspected ISAR images (82.14% for the Boeing 737 and 85.71% for the Boeing 727), those obtained by using the proposed algorithm are better focused

than those obtained by using the conventional ISAR autofocusing algorithm.

2) *Ships*: The ISAR images of the bulk carrier obtained by using the FMCW and the conventional autofocusing algorithms are shown in Fig. 14, whereas those relative to the bulk loader are shown in Fig. 15. The range and Doppler sections relative to the highlighted scattering centres of the bulk carrier (in Fig. 14) are shown in Fig. 16, whereas relative to the bulk loader they are shown in Fig. 17.

The peak, the IC values and the Entropy (E) values of the ISAR images in Fig. 14 and Fig. 15 are shown in Table VI. The IP and IC are higher when using the FMCW autofocusing algorithms in both cases.

The difference between  $IC_{FMCW}$  and  $IC_{Pulsed}$  is shown for both the bulk carrier and the bulk loader in Fig. 18. The time window used to obtain the ship ISAR images is 96 sweeps long with a shift of 32 sweeps at each step. In Fig. 18, the black line

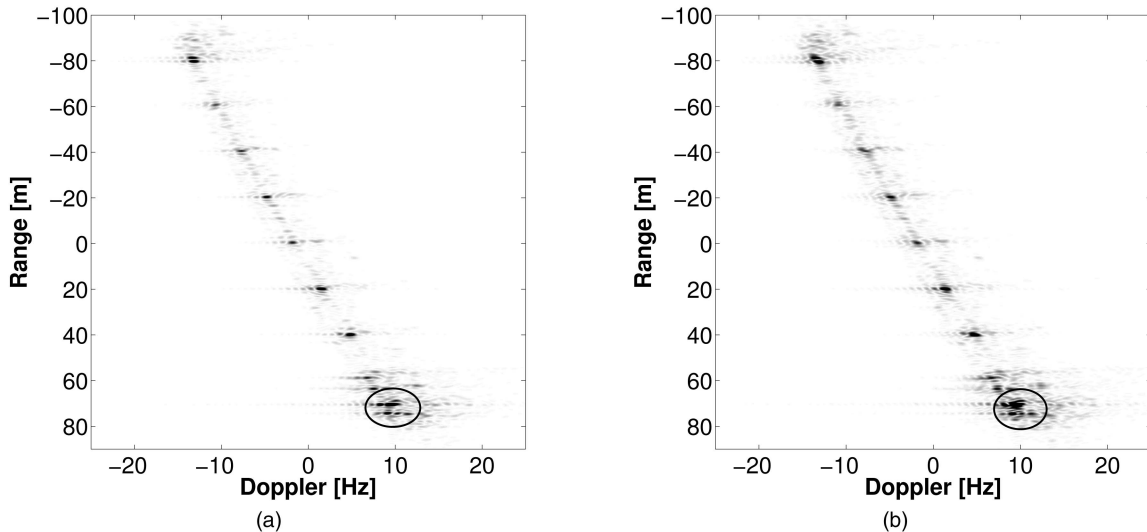


Fig. 14. Bulk carrier ISAR images obtained by using FMCW ISAR autofocusing algorithm (a) and conventional autofocusing algorithm (b).

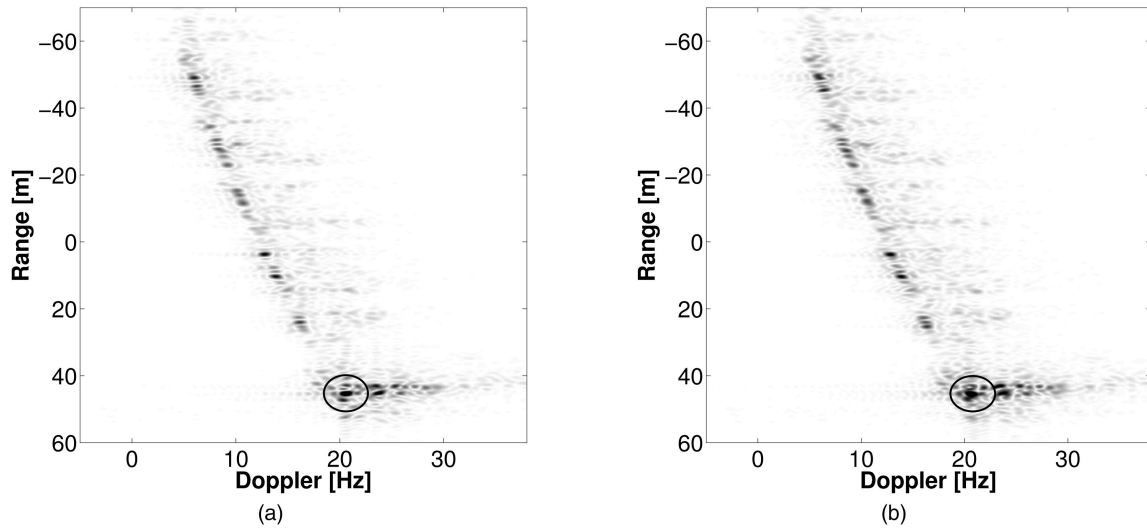


Fig. 15. Bulk loaderISAR images obtained by using FMCW ISAR autofocusing algorithm (a) and conventional autofocusing algorithm (b).

represents the difference between  $IC_{FMCW}$  and  $IC_{Pulsed}$  and the dashed line represents the mean value of such difference.

The results in Fig. 18 show that for almost all the inspected ISAR images, specifically 97.39% for the bulk carrier and 93.09% for the bulk loader, the ISAR images obtained by using the proposed algorithm are better focused than those obtained by using the conventional ISAR autofocusing algorithm.

## VI. CONCLUSIONS

The theoretical aspects of FMCW ISAR imaging have been investigated in detail in this paper. Specifically the problem of ISAR image formation when using FMCW radars has been studied analytically and a closed-form derivation of the ISAR system PSF has been obtained. A suitable

processing for FMCW ISAR image autofocusing has been proposed and applied to both simulated and real data in order to prove its effectiveness. Moreover, differences between pulsed and FMCW ISAR have been pointed out throughout the paper. The data used to test the algorithm are stepped frequency waveforms. The equations of the FMCW radar can be used in stepped frequency radar because the stepped frequency radar is a piecewise approximation of the linear FMCW radar, therefore, the assumption of stop&go is not valid. Therefore, the target radial motion within the sweep must be taken into account in the same manner as for FMCW radar. As observed in Section V, the target motion within the sweep produce a PSF spreading mostly along the range coordinate. Such defocusing effect can be compensated by means of the proposed algorithm.

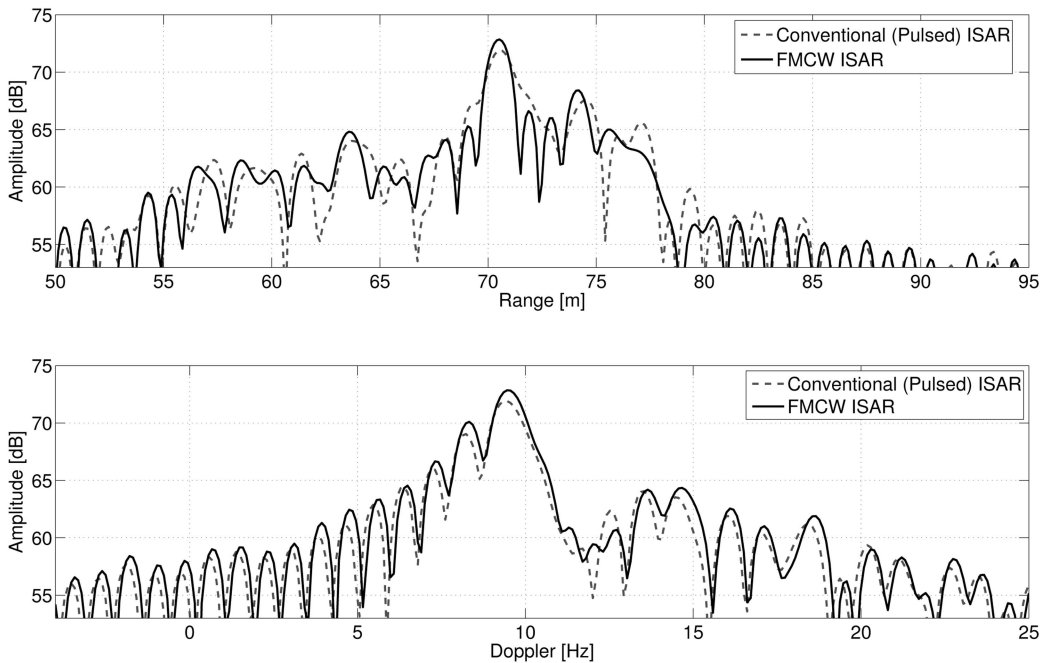


Fig. 16. Range and Doppler sections of Fig. 14 (a)–(b).

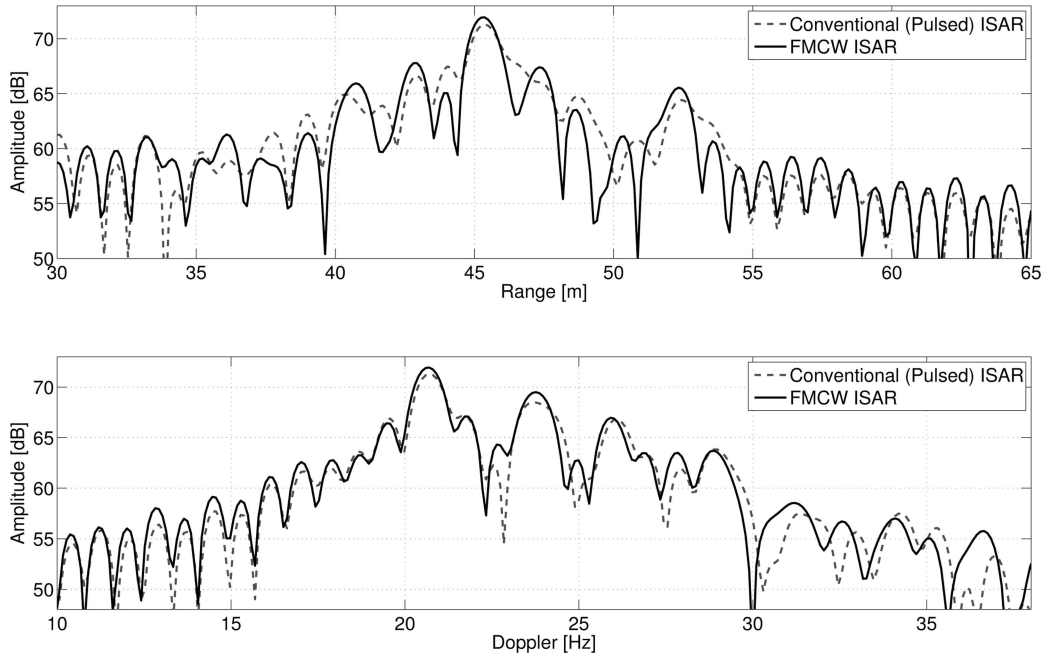


Fig. 17. Range and Doppler sections of Fig. 15 (a)–(b).

In fact, an extended analysis on a large number of ISAR images, has demonstrated that in most cases the proposed algorithm performs better than the conventional ISAR autofocusing algorithm in terms of IC.

Even though the differences between the ISAR images obtained by using the FMCW ISAR autofocusing algorithm and the conventional ISAR autofocusing algorithm are not always visibly perceptible, it is important to remember that the FMCW ISAR autofocusing algorithm does not require

a computational load higher than that of the pulsed ISAR.

#### ACKNOWLEDGMENT

The authors would like to thanks the Defence Science and Technology Organisation (DSTO) for releasing real data.

#### APPENDIX

- 1) *Derivation of the Phase Term due to the Target Radial Motion:* Mathematical details for the derivation of (25) are provided.

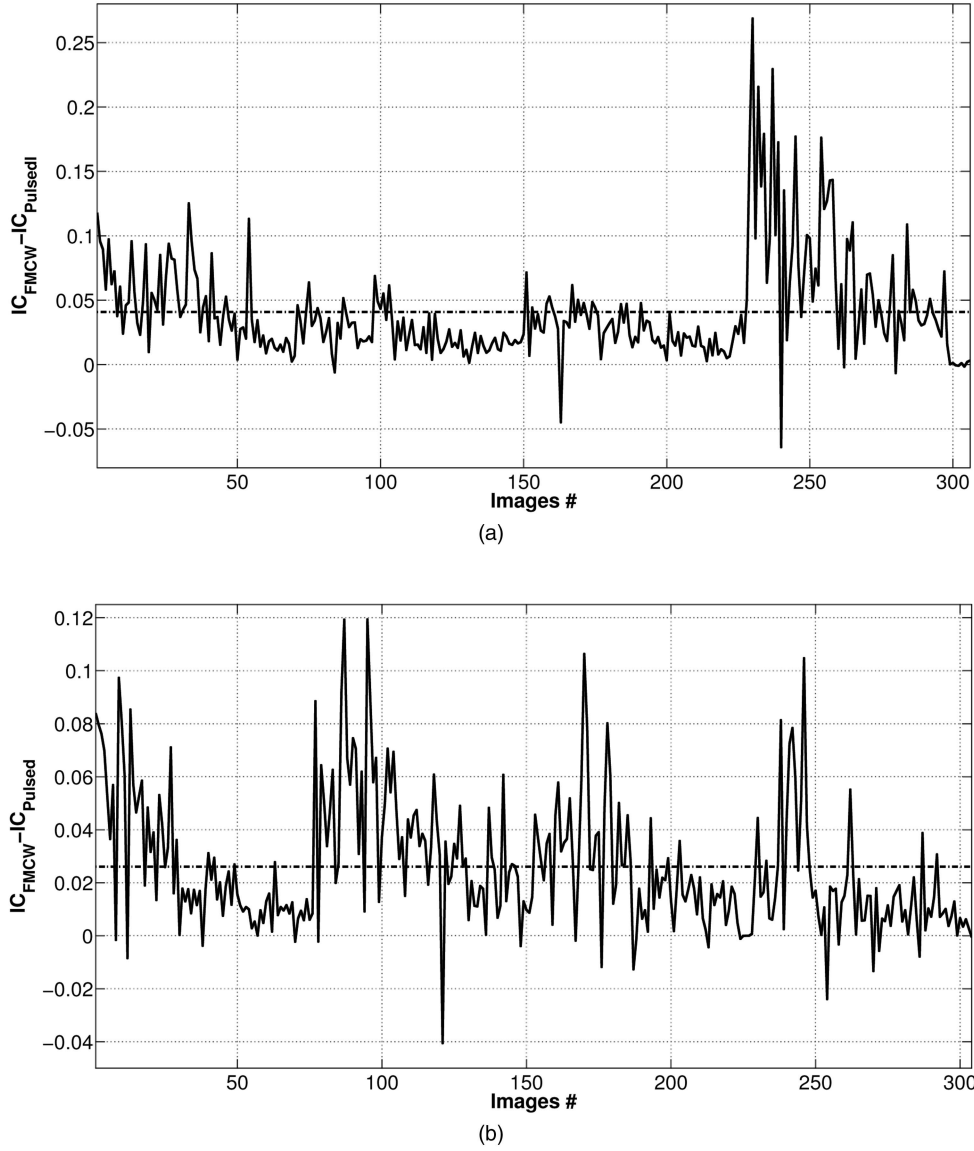


Fig. 18. Difference between  $IC_{FMCW}$  and  $IC_{Pulsed}$  for (a) bulk carrier and for (b) bulk loader.

By using (8) and (16), (22) can be written as follows:

$$\begin{aligned}\phi_0(t_s, n) = & -2\pi(f_c + \alpha t_s) \cdot \left( \tau_0(n) + \frac{2}{c} v_r(n) t_s \right) \\ & - \pi \alpha \left( \tau_0(n) + \frac{2}{c} v_r(n) t_s \right)^2.\end{aligned}$$

By defining  $f_D(n) = 2f_c v_r(n)/c$  and  $f_b(n) = \alpha \tau_0(n)$  as in (27) and (28)  $\phi_0(t_s, n)$  can be rewritten as

$$\begin{aligned}\phi_0(t_s, n) = & -2\pi f_c \tau_0(n) - 2\pi f_b(n) t_s - 2\pi f_D(n) t_s \\ & - \pi \alpha t_s^2 \frac{f_D(n)}{f_c} \left( 2 - \frac{f_D(n)}{f_c} \right) \\ & + \pi \alpha \tau_0^2(n) + 2\pi f_b(n) \frac{f_D(n)}{f_c} t_s.\end{aligned}$$

When the inequality  $f_D(n) \ll f_c$  is satisfied  $\phi_0(t_s, n)$  can be rewritten as follows

$$\begin{aligned}\phi_0(t_s, n) \approx & -2\pi f_c \tau_0(n) - 2\pi f_b(n) t_s - 2\pi f_D(n) t_s \\ & - 2\pi \alpha t_s^2 \frac{f_D(n)}{f_c} + \pi \alpha \tau_0^2(n) + 2\pi f_b(n) \frac{f_D(n)}{f_c}.\end{aligned}$$

Moreover

$$\begin{aligned}\phi_0(t_s, n) \approx & -2\pi f_c \tau_0(n) - 2\pi f_b(n) t_s \left( 1 - \frac{f_D(n)}{f_c} \right) \\ & - 2\pi f_D(n) t_s - 2\pi \alpha t_s^2 \frac{f_D(n)}{f_c} + \pi \alpha \tau_0^2(n)\end{aligned}$$

therefore (25) is derived

$$\begin{aligned}\phi_0(t_s, n) \approx & -2\pi f_c \tau_0(n) - 2\pi f_b(n) t_s - 2\pi f_D(n) t_s \\ & - 2\pi \alpha t_s^2 \frac{f_D(n)}{f_c} + \pi \alpha \tau_0^2(n).\end{aligned}$$

2) *Support Band Derivation:* Mathematical details for the derivation of (35), (36), and (37) are provided.

By using (23), (24), and (9) it is possible to deduce

$$\begin{aligned}\phi_1(t_S, n, \mathbf{x}) + \phi_2(t_S, n, \mathbf{x}) \\ = -2\pi \cdot \frac{2}{c} \mathbf{x}^T \cdot \mathbf{i}_{\text{LOS}}(t_S, n) \\ \cdot \left[ f_c + \alpha \left( t_S - \frac{\tau'(t_S, n, \mathbf{x})}{2} \right) \right]\end{aligned}$$

moreover by using (34)

$$\begin{aligned}\phi_1(t_S, n, \mathbf{x}) + \phi_2(t_S, n, \mathbf{x}) \\ = -2\pi \frac{2}{c} [x_1 \cos(\theta(t_S, n)) + x_2 \sin(\theta(t_S, n))] \\ \cdot \left[ f_c + \alpha \left( t_S - \frac{\tau'(t_S, n, \mathbf{x})}{2} \right) \right].\end{aligned}$$

Therefore by defining

$$\begin{aligned}X_1(t_S, n) = \left\{ f_c + \alpha \left[ t_S - \tau_0(n) - \frac{\tau'(t_S, n, \mathbf{x}')}{2} \right] \right\} \\ \cdot \frac{2}{c} \cos(\theta(t_S, n))\end{aligned}$$

and

$$\begin{aligned}X_2(t_S, n) = \left\{ f_c + \alpha \left[ t_S - \tau_0(n) - \frac{\tau'(t_S, n, \mathbf{x}')}{2} \right] \right\} \\ \cdot \frac{2}{c} \sin(\theta(t_S, n))\end{aligned}$$

the expression of  $S_{bc}(t_S, n)$  is derived.

## REFERENCES

- [1] Charvat, G. L. and Kempel, L. C.  
Synthetic aperture radar imaging using a unique approach to frequency-modulated continuous-wave radar design.  
*IEEE Antennas and Propagation Magazine*, **48** (2006), 171–177.
- [2] Nouvel, J. F., Roques, S., and du Plessis, O. R.  
A low-cost imaging radar: Drive on board ONERA motorglider.  
In *Proceedings of the IEEE International Geoscience and Remote Sensing Symposium (IGARSS 2007)*, 2007, 5306–5309.
- [3] Meta, A., Hoogeboom, P., and Ligthart, L. P.  
Signal processing for FMCW SAR.  
*IEEE Transactions on Geoscience and Remote Sensing*, **45**, 11 (2007), 3519–3532.
- [4] Edrich, M. and Weiss, G.  
Second-generation ka-band UAV SAR system.  
In *Proceedings of the European Radar Conference (EuRAD 2008)*, 2008, 479–482.
- [5] de Wit, J. J. M., Meta, A., and Hoogeboom, P.  
Modified range-Doppler processing for FM-CW synthetic aperture radar.  
*IEEE Geoscience and Remote Sensing Letters*, **3** (Jan. 2006), 83–87.
- [6] Burgos-Garcia, M., Perez-Martinez, F., and Menoyo, J. G.  
Radar signature of a helicopter illuminated by a long LFM signal.  
*IEEE Transactions on Aerospace and Electronic Systems*, **45** (2009), 1104–1110.
- [7] Ausherman, D. A., et al.  
Developments in radar imaging.  
*IEEE Transactions on Aerospace and Electronic Systems*, **AES-20** (1984), 363–400.
- [8] Walker, J. L.  
Range-Doppler imaging of rotating objects.  
*IEEE Transactions on Aerospace and Electronic Systems*, **AES-16** (1980), 23–52.
- [9] Haywood, B. and Evans, R. J.  
Motion compensation for ISAR imaging.  
In *Proceedings of ASSPA 89*, Adelaide, Australia, 1989, 113–117.
- [10] Berizzi, F., et al.  
A survey on ISAR autofocusing techniques.  
In *Proceedings of the IEEE ICIP 2004*, Singapore, 2004.
- [11] Xi, L., Gousui, L., and Ni, J.  
Autofocusing of ISAR images based on entropy minimization.  
*IEEE Transactions on Aerospace and Electronic Systems*, **35** (1999), 1240–1252.
- [12] Martorella, M., Berizzi, F., and Haywood, B.  
A contrast maximization based technique for 2D ISAR autofocusing.  
*IEE Proceedings—Radar, Sonar and Navigation*, **152**, 4 (2005), 253–262.
- [13] Wang, Y., Ling, H., and Chen, V. C.  
SAR motion compensation via adaptive joint time-frequency technique.  
*IEEE Transactions on Aerospace and Electronic Systems*, **34** (Apr. 1998), 670–677.
- [14] Lei, W., Long, T., and Han, Y.  
Moving targets imaging for stepped frequency radar.  
In *Proceedings of the 5th International Conference on Signal Processing (WCCC-ICSP 2000)*, vol. 3, 2000, 1851–1855.
- [15] Berizzi, F., et al.  
A contrast-based algorithm for synthetic range-profile motion compensation.  
*IEEE Transactions on Geoscience and Remote Sensing*, **46**, 10 (2008), 3053–3062.
- [16] Martorella, M.  
Novel approach for ISAR image cross-range scaling.  
*IEEE Transactions on Aerospace and Electronic Systems*, **44**, 1 (2008), 281–294.
- [17] Karakasiliotis, A., et al.  
Two-dimensional ISAR model and image reconstruction with stepped frequency modulated signal.  
*IET Signal Processing* (special Issue on ISAR), **2**, 3 (2008), 277–290.
- [18] Berizzi, F., et al.  
High-resolution ISAR imaging of maneuvering targets by means of the range instantaneous Doppler technique: Modeling and performance analysis.  
*IEEE Transactions on Image Processing*, **10** (2001), 1582–1588.
- [19] Carrara, W. C., Goodman, S., and Majewsky, R. M.  
*Spotlight Synthetic Aperture Radar: Signal Processing Algorithms*.  
Norwood, MA: Artech House, 1995.
- [20] Meta, A. and Hoogeboom, P.  
Signal processing algorithms for FMCW moving target indicator system aperture radar.  
In *Proceedings of the IEEE International Symposium on Geoscience and Remote Sensing (IGARSS 2005)*, Seoul, Korea, July 2005, 316–319.

- [21] Berizzi, F., et al.  
Use of 3D scatterer models from ISAR image sequences  
for target recognition.  
*Elsevier DSP*, **16** (2006), 523–532.
- [22] Martorella, M. and Berizzi, F.  
Time windowing for highly focused ISAR image  
reconstruction.  
*IEEE Transactions on Aerospace and Electronic Systems*,  
**41** (2005), 992–1007.



**Elisa Giusti** was born in Pisa, Italy, in April 1982. She received the Italian Laurea (M.S.) degree in telecommunication engineering from the University of Pisa, Pisa, Italy in October 2006.

Since January 2007 she has been a Ph.D. student with the Department of Information Engineering at the same university. Her research interests are in the field of signal processing and polarimetric inverse synthetic aperture radar.

**Marco Martorella** (M'99—SM'09) was born in Portoferraio, Italy in June 1973. He received the Telecommunication Engineering Laurea (cum laude) and Ph.D. degrees from the University of Pisa, Italy in 1999 and 2003, respectively.

He became a postdoctoral researcher in 2003, a researcher/lecturer in 2005 and a permanent senior researcher/lecturer in 2008 at the Department of Information Engineering of the University of Pisa. He has been a regular visitor of the Department of Electrical and Electronic Engineering of the University of Melbourne, the Department of Electrical and Electronic Engineering of the University of Adelaide and the Department of Information Technology and Electrical Engineering of the University of Queensland since 2001. His research interests are mainly in the field of radar imaging.

Dr. Martorella has coauthored more than 20 journal papers and 40 conference papers. He has given lectures and seminars in several research institutions in the U.S., Australia, South Africa, Asia, and Europe and presented tutorials on ISAR at IEE/IEEE Radar Conferences. He received the Australia-Italy award for young researchers in 2008.

